PCCP

PAPER

View Article Online
View Journal | View Issue

Cite this: *Phys. Chem. Chem. Phys.*, 2015, **17**, 24412

Hybrid zinc oxide/graphene electrodes for depleted heterojunction colloidal quantum-dot solar cells†

Mohammad Mahdi Tavakoli,[ab] Hossein Aashuri,[a] Abdolreza Simchi*[ac] and Zhiyong Fan[b]

Received 20th June 2015,
Accepted 18th August 2015

DOI: 10.1039/c5cp03571f

www.rsc.org/pccp

Recently, hybrid nanocomposites consisting of graphene/nanomaterial heterostructures have emerged as promising candidates for the fabrication of optoelectronic devices. In this work, we have employed a facile and *in situ* solution-based process to prepare zinc oxide/graphene quantum dots (ZnO/G QDs) in a hybrid structure. The prepared hybrid dots are composed of a ZnO core, with an average size of 5 nm, warped with graphene nanosheets. Spectroscopic studies show that the graphene shell quenches the photoluminescence intensity of the ZnO nanocrystals by about 72%, primarily due to charge transfer reactions and static quenching. A red shift in the absorption peak is also observed. Raman spectroscopy determines G-band splitting of the graphene shell into two separated sub-bands (G^+, G^-) caused by the strain induced symmetry breaking. It is shown that the hybrid ZnO/G QDs can be used as a counter-electrode for heterojunction colloidal quantum-dot solar cells for efficient charge-carrier collection, as evidenced by the external quantum efficiency measurement. Under the solar simulated spectrum (AM 1.5G), we report enhanced power conversion efficiency (35%) with higher short current circuit (80%) for lead sulfide-based solar cells as compared to devices prepared by pristine ZnO nanocrystals.

Introduction

Fabrication of thin film solar cells utilizing solution-based processes has gained increasing attention due to lower processing costs and reduced material utilization.[1,2] Recently, depleted bulk heterojunction (DBH) colloidal quantum-dot solar cells based on lead sulfide (PbS) QDs have emerged as a promising class of devices, with potential for low cost processing[3,4] and tuneable bandgap engineering.[5] Interest in the field of PbS QD photovoltaics has surged, promoted by the observation that short ligands and atomic passivation of QDs can increase the carrier mobility in thin films by several orders of magnitude.[6,7]

It has recently been shown that employing a solid-state ligand exchange procedure, wherein the long-chain ligand oleic acid (which is commonly used in the QD synthesis) is replaced with 1,2-ethanedithiol, can ramp up the power conversion efficiency (PCE) value to about 8.5%.[8] Much effort has also been made to increase the PCE by developing structured electrodes for charge carrier collection. In this regard, Lan *et al.*[9] have developed a self-assembled nanowire network for DBH PbS CQD solar cells to improve the PCE by >15% as compared to electrodes with a planar structure. Pyramid-shaped electrodes employed in a hierarchically structured device have also been made by Labelle *et al.*[10] in order to improve light absorption, and thus the PCE. A more recent strategy is to deal with efficient electron ejection, which is always desirable in competing with carrier trapping and even thermalization/cooling. In this case, some efforts have been devoted to the preparation of one-dimensional TiO_2[9] and ZnO[11] nanostructures to enhance charge-carrier collection.

More recently, graphene, one atom-thick and a honeycomb lattice made of carbon atoms, and its hybrid materials with nanoparticles have been found to be of great interest for photoelectrodes and energy harvesting due to the fact that they can operate as a fast electron funnel.[12–14] For efficient and fast extraction of charge carriers, graphene is a very promising material. Konstantatos *et al.*[15] fabricated hybrid PbS/G photodetectors consisting of a monolayer or bilayer of graphene covered with a thin film of colloidal PbS QDs, with ultrahigh gain ($\sim 10^8$ electrons per photoanode responsivity of $\sim 10^7$ A W^{-1}). Zhang *et al.*[16] prepared single-layer graphene transistors by the chemical vapour deposition method. They demonstrated improved

[a] *Department of Materials Science and Engineering, Sharif University of Technology, 14588 Tehran, Iran. E-mail: simchi@sharif.edu; Fax: +98 (21) 6600 5717; Tel: +98 (21) 6616 5261*
[b] *Department of Electronic and Computer Engineering, Hong Kong University of Science and Technology, Clear Water Bay, Kowloon, Hong Kong*
[c] *Institute for Nanoscience and Nanotechnology, Sharif University of Technology, 14588 Tehran, Iran*

† Electronic supplementary information (ESI) available. See DOI: 10.1039/c5cp03571f

sensitivity to light upon deposition of PbS films with different thicknesses by electron beam evaporation. Eck *et al.*[17] could increase the PCE of hybrid polymer solar cells up to 4.2% by incorporating CdSe QDs/thiolated reduced graphene oxide (rGO) into the devices. We have also recently reported the potential of hybrid PbS/G structures to enhance charge-carrier collection in CQD solar cells.[18] In our work, the hybrid nanostructure was prepared by *in situ* deposition of PbS QDs on graphene sheets by a supercritical method. In a related work, Son *et al.*[19] fabricated solar cell devices by employing ZnO/G QDs, a hybrid structure, as an absorber layer and achieved a PCE of 2.33%. Recently, Wang *et al.*[20] used nanocomposites of graphene and TiO_2 nanoparticles as the electron collection layer in meso-superstructured perovskite solar cells. They employed graphene nanoflakes, which provide superior charge collection in the nanocomposites and attained a remarkable photovoltaic performance, with a PCE up to 15.6%. Zhu *et al.*[21] also improved the PCE of perovskite solar cells from 8.81% to 10.15% through the insertion of an ultrathin graphene quantum dot layer between the perovskite and TiO_2 layers, resulting in fast extraction of the carriers.

Here, we have employed hybrid ZnO/G QDs to prepare counter-electrodes for CQD solar cells based on PbS nanocrystals. Quasi ZnO/G hybrid QDs are prepared by an *in situ* chemical processing of ZnO nanoparticles in the presence of graphene oxide nanosheets. In the presence of a reducing agent, the nucleated ZnO nanocrystals are warped with a graphene nanoshell, yielding a hybrid nanostructure. The CQD solar cells are then prepared by spin coating and solid-state ligand exchange processes, followed by evaporation and sputtering of the top contacts. It is shown that the devices prepared from the hybrid ZnO/G nanostructures yield higher power conversion efficiency than those prepared from TiO_2 and ZnO electrodes. We suggest that this improvement is attained by enhanced separation and transport of charge carriers to the collecting electrodes through static quenching.

Results

Characterization of quantum dots

The characteristics of hybrid ZnO/G QDs were studied by high resolution transmission electron microscopy (HRTEM), Raman spectroscopy and X-ray photoelectron spectroscopy (XPS). Typical results are presented in Fig. 1. Fig. 1(a) shows ultrafine particles with an average size of about 5 nm (more TEM images of these particles can be found in the ESI,† Fig. S1). It seems that ZnO/G QDs have a core/shell structure, as shown in Fig. S2a (ESI†). The EDS analysis supports the conclusion that the particles are composed of zinc oxide and graphene materials (ESI,† Fig. S2). The HRTEM study of the particles (Fig. 1(b)) indicates that the core has an interplanar spacing of 0.26 nm, which corresponds to the distance between two (002) planes of the hexagonal structure of zinc oxide with preferential growth along the [002] direction (*c* axes),[22] which is in a good agreement with the HRTEM image of the ZnO QDs (ESI,† Fig. S3). The shell has an interplanar spacing of 0.14 nm, matching the atomic distance of monolayer graphene (hexagonal atomic lattice).[14]

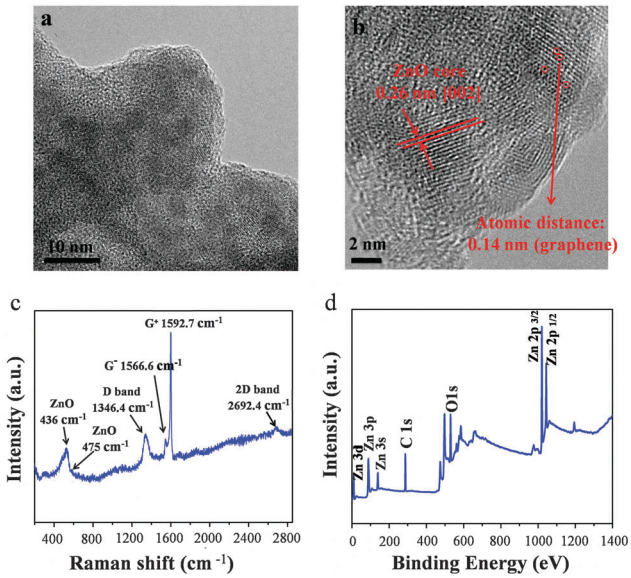

Fig. 1 Characterization of hybrid ZnO/G quantum dot prepared by *in situ* chemical procesing of ZnO nanocrystals in the presence of GO nanosheets. (a and b) HRTEM images show a hybrid structure of ZnO quantum dots/graphene nanosheets. (c) Raman spectra indicate G peak splitting of the graphene shell. (d) XPS spectra of hybrid ZnO/G QDs show binding energy of emitted electrons from zinc and oxygen in ZnO structure and C in graphene.

The Raman spectra of the hybrid QDs (Fig. 1(c)) show a double degenerate G peak splitting into two sub-bands, namely G^+ (1592.7 cm^{-1}) and G^- (1566.6 cm^{-1}), for the graphene nanoshell. This G-band splitting is most probably caused by the strain induced symmetry breaking[22] upon bending of the graphene layer surrounding the ZnO nanocrystals. In addition, the presence of a D-band at 1346.4 cm^{-1} points out the presence of defects and disorders in the graphitic sheets. Nevertheless, the position of a sharp 2D peak at 2692.4 cm^{-1} could support the formation of an ultrathin graphene shell upon chemical processing.[14] XPS analysis (Fig. 1(d)) indicates the bonding energies for emitted electrons at 1022.38 ($Zn2p_{3/2}$), 531.8 (O1s) and 284.6 eV (C1s). The strong O1s peak belongs to the lattice oxygen in ZnO,[23] while the C1s spectra are related to the carbon element in association with oxygen in GO.[24]

The optical properties of the hybrid ZnO/G QDs as compared to pristine ZnO nanoparticles are shown in Fig. 2. Ultraviolet-visible (UV-Vis) spectra shows that the absorption peak for both materials is located in the UV region (Fig. 2(a)); nevertheless, the hybrid dots exhibit an auxiliary enhanced absorption edge to longer wavelengths (a red shift of *ca.* 25 nm) due to the size effect. As shown in Fig. S4 (ESI†) and Fig. 1(b), the ZnO core in the ZnO/G QDs becomes larger to some extent because of different synthesis conditions. PL measurement also determines a luminescence quenching effect of the graphene shell by about 72% (Fig. 2(b)).

The results of the imaging and spectroscopic techniques employed to characterize the Cd-doped PbS QDs are summarized in Fig. 3. The HRTEM images show that the nanocrystals have an average size of $\sim$3 nm, with a narrow size distribution (Fig. 3(a)).

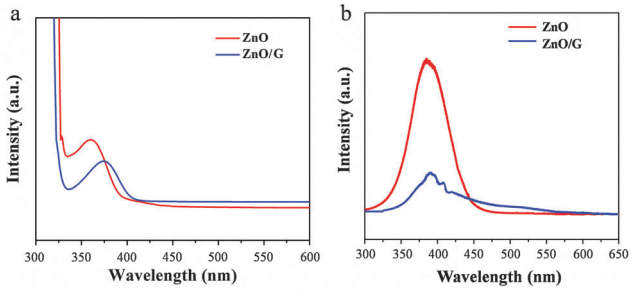

Fig. 2 Optical properties of hybrid ZnO/G QDs as compared to pristine ZnO nanoparticles. (a) UV-Vis spectrum of the colloidal solutions in DMF (24 mg ml^{-1}). (b) PL spectrum of CQD films (300 nm) prepared by spin coating.

The interplanar spacing is 0.295 nm (Fig. 3(b)), which corresponds to the distance between the (200) planes of the cubic lead sulfide structure. The formation of crystalline lead sulfide is further supported by the selected area electron diffraction (SAED) pattern (Fig. 3(c)) and EDS (ESI,† Fig. S5). The XRD pattern of the QDs also fits well with cubic lead sulfide (JCPDS 02-0699) (Fig. 3(d)). UV-Vis spectroscopy illustrates a well-defined excitonic peak at 920 nm, which corresponds to an optical bandgap of 1.34 eV (Fig. 3(e)). A strong PL peak at 1100 nm (under excitation at 405 nm) is also obtained, which is beneficial in terms of improved near-infrared absorption of the solar spectrum (Fig. 3(f)). Nevertheless, the full width at half maximum (FHWM) of the PL peak is relatively large (about 40 nm), which indicates the size distribution of the colloidal nanoparticles.

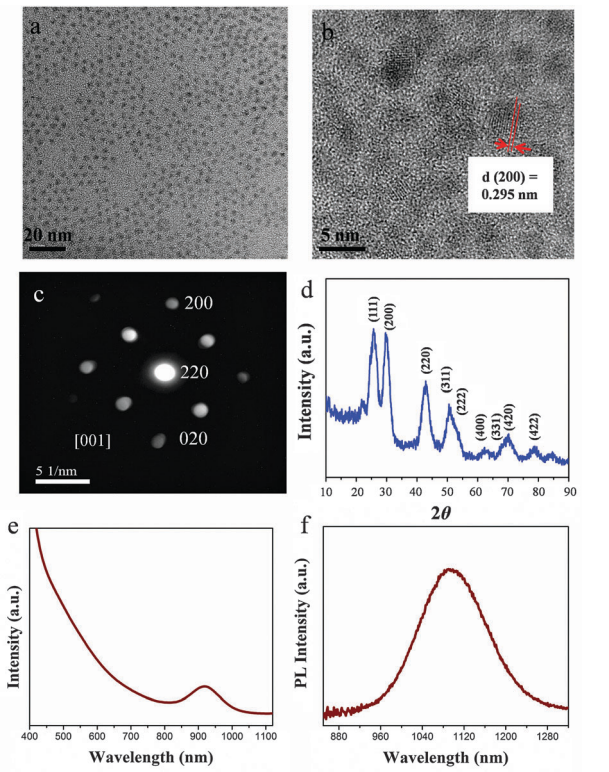

Fig. 3 Characterization of Cd-doped PbS QDs. (a and b) HRTEM images show uniform nanocrystals with an average size of ~3 nm. (c) SAED and (d) XRD patterns support the formation of PbS nanocrystals with a cubic lattice structure. (e) UV-Vis spectroscopy indicates an absorption peak at 920 nm, which corresponds to an optical bandgap of 1.34 eV. (f) PL measurement shows a single but Gaussian-shaped peak (inhomogeneous broadening) at around 1100 nm.

Characterization of the electrodeposited hybrid film

To prepare the counter-electrode, EPD of the hybrid ZnO/G QDs was performed. Fig. 4(a) shows a top-view FESEM image of the ZnO/G QD film deposited on the FTO/c-TiO_2 substrate. The film is dense and uniform. The XRD pattern of the film (Fig. 4(b)) indicates that the ZnO nanoparticles are fully crystalline with Bragg peaks of standard bulk zinc oxide (JCPDS no. 36-1451). The presence of graphene in the film is supported by the appearance of a (002) broad intense peak centered at 25.9° and a (100) broad peak at 43.6° with low intensity. Fig. 4(c) shows the effect of ZnO/G film thickness on the optical transmittance of FTO glass measured over the wavelength of 300-800 nm. Although the absorbance of a single graphene sheet is less than 2%,[14] the results indicate that the hybrid films significantly reduce the optical transmittance of FTO glass at a thickness of few hundred nanometers. Meanwhile, the transmittance is similar to that of ZnO and TiO_2-coated FTO substrates at a thickness of 100 nm.

Photovoltaic performance

Fig. 5(a) shows a cross-sectional FESEM image of DBH PbS-based solar cells fabricated on the hybrid ZnO/G QD film. The thickness of the absorbing layer is about 300 nm. The current density–voltage (*J–V*) curves of the solar cell devices under simulated 1.5 AMG sun spectra are illustrated in Fig. 5(b). To illustrate the

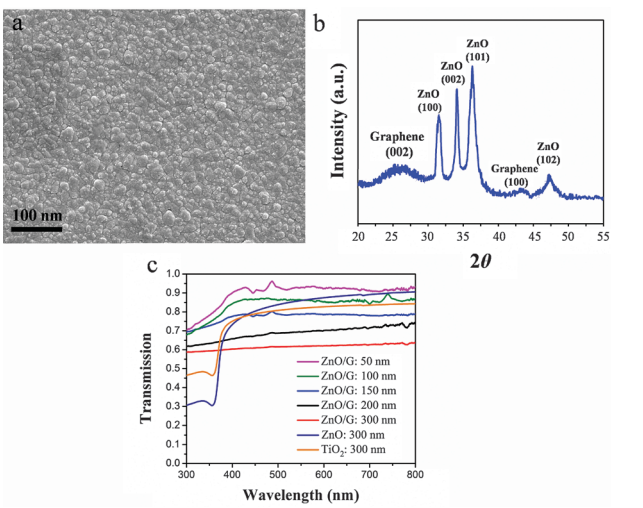

Fig. 4 Characterization of hybrid ZnO/G film prepared by EPD. (a) SEM image shows that the film is completely dense and uniform, and composed of ultrafine particles. (b) XRD pattern indicates that the particles are mainly composed of crystalline ZnO (JCPDS no. 36-1451). Two weak and broad characteristic peaks of graphene are also detectable in the XRD pattern. (c) Effect of film thickness on the transmittance of hybrid ZnO/G layers.

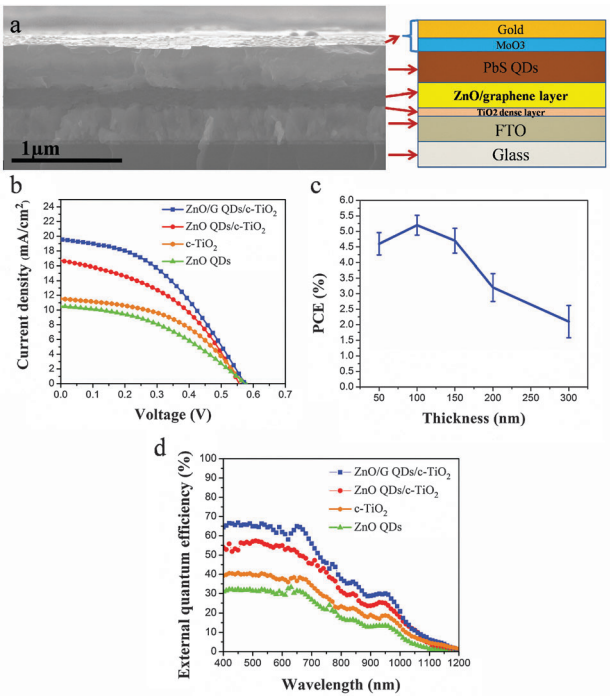

Fig. 5 (a) Cross-sectional SEM image illustrating the structure of DBH QD solar cells prepared by a combined electrophoretic deposition of hybrid ZnO/G QDs and spin coating of PbS nanocrystals. (b) *J*–*V* curves under 1.5 AMG indicating the photovoltaic performance of the heterojunction devices. (c) The effect of hybrid film thickness on the PV performance of DBH solar cells prepared by employing the hybrid ZnO/G electrode. (d) EQE spectra determining the role of different types of electrodes on the quantum efficiency of the PbS QD film.

potential of the hybrid ZnO/G electrode, the *J*–*V* sweeps for the other substrates, FTO/ZnO, FTO/c-TiO_2 and FTO/c-TiO_2/ZnO, are presented. Table 1 summarizes the figures of merit for the examined devices (for n = 10). We have obtained on average 5.7 ± 0.3% PCE for the hybrid ZnO/G counter-electrode with a 100-nm-thick hybrid film. It is notable from Fig. 5c that the thickness of the hybrid ZnO/G layer affects the PV performance as there is a counterbalance between the charge extraction and light transmittance (Fig. 4(c)). In the optimum case, the PCE is improved by 35% compared to the c-TiO_2/ZnO electrode (PCE = 4.5% ± 0.2) and even more as compared with the two other substrates. This improvement is mainly achieved by the higher short current density (J_{sc}) and the fill factor (FF) of the hybrid devices. The external quantum efficiency (EQE) spectra of different devices are shown in Fig. 5(d). In agreement with the *J*–*V* measurements, the device based on the hybrid ZnO/G QDs exhibits higher EQE and current density.

Table 1 Figures of merit for the prepared PbS QD solar cells based on different types of electrodes (n = 10)

Electrode	V_{oc} (V)	J_{sc} (mA cm^{-2})	FF (%)	PCE (%)
ZnO/G QDs/c-TiO_2	0.58 ± 0.04	19.7 ± 1.2	50 ± 3	5.7 ± 0.3
ZnO QDs/c-TiO_2	0.56 ± 0.07	16.8 ± 1.8	48 ± 4	4.5 ± 0.2
c-TiO_2	0.56 ± 0.03	11.6 ± 1.3	55 ± 2	3.47 ± 0.2
ZnO QDs	0.57 ± 0.08	10.4 ± 2.4	50 ± 3	2.9 ± 0.4

We used the ZnO/G QD structure as a fast electron extraction layer in the PbS QD solar cell in order to improve the carriers' mobility and, as a result, the current density. Fig. 6(a) and (b) schematically shows the architecture of the device for fast carrier transfer. It can be noted that the device with this configuration illustrates the highest current density and PCE compared with other devices that do not use graphene. In Fig. 6(c), the band diagram of the PbS QD solar cell based on a ZnO/G layer is plotted. In order to study the thin layer of ZnO/G QDs (100 nm) the work function and valence band energy of the ZnO/G QDs were measured by ultraviolet photoelectron spectroscopy (UPS) (Fig. 6(d)). He I (21.2 eV) was utilized as a photon source for UPS measurements. The band gap of ZnO/G QDs was calculated by using the absorption spectrum recorded using a UV-vis spectroscope (Fig. 2(a)). The conduction band of the ZnO/G QDs was calculated from the difference between their measured valence band and the band gap. Based on these values, the energy band diagram of the ZnO/G QDs was estimated. As can be seen in Fig. 6(c), the ZnO/G QD layer matches the PbS QD layer very well. This is because the electrons are transferred from the absorber layer to the ZnO QDs easily within the graphene nanoshells. Here, the depleted region is formed between PbS QD and ZnO/G QD layers.

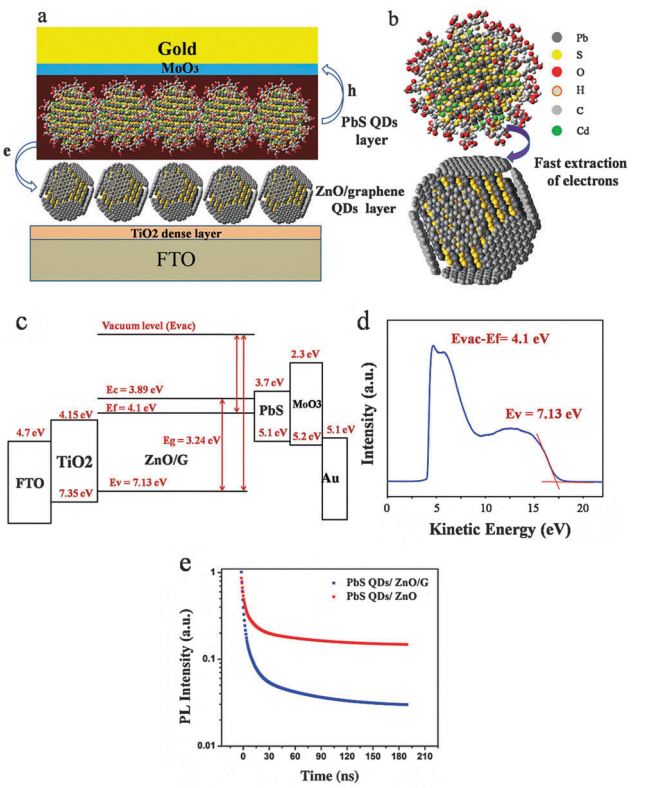

Fig. 6 (a) Schematic of a PbS QD solar cell fabricated on a ZnO/G QD film, which works as a fast electron extraction layer. (b) Schematic of Cd-doped PbS QDs and ZnO/G QDs. (c) Band diagram of the device based on ZnO/G QDs. (d) ZnO/G QDs' work function measured using the ultraviolet photoelectron spectrum (UPS). (e) Time-resolved PL spectra of the PbS QD layer (100 nm thickness) deposited on the hybrid ZnO/G (blue curve) and pristine ZnO (red curve) films (100 nm thickness).

Table 2 Fitting parameters of the corresponding PL decay curves

Electrode	τ (ns)	β_1	β_2	β_3	χ
ZnO	10	15872.6	6848.4	2220.6	1.03
ZnO/G	1.2	16727.5	3968.8	629.4	1.05

Thus, in this region, graphene may improve the electrical field and, as a result, the mobility of electrons. Fig. 6(e) shows the results of time resolved photoluminescence measurements. Table 2 shows the fitting parameters of the corresponding PL decay curves. The quenched spectrum of the ZnO QDs in the presence of the graphene shell is primarily caused by the charge transfer reactions and static quenching. Despite the dynamic quenching, when the donor and acceptor materials are in the ground state, static quenching occurs, thereby improving the carrier extraction.

Discussion

The chemical synthesis of ZnO nanoparticles in dimethylformamide (DMF) is performed according to eqn (1):[22]

$$Zn(CH_3COO)_2{\cdot}H_2O + (CH_3)_2NC(O)H \rightarrow ZnO + (CH_3COO)_2CHN(CH_3)_2 + H_2O \quad (1)$$

In the presence of GO nanosheets, two chemical reactions are likely to occur at the surface of the embryonic ZnO QDs:[22] (1) Zn^{2+} ions are chemisorbed on the surface of the embryonic ZnO QDs and react with the GO functional groups to form Zn–O–C bonds; and (2) Zn^{2+} ions bonded to GO establish Zn–O bonds and combine with embryonic ZnO QDs. During these reactions, the graphene nanoshells are detached from the GO nanosheets through a layer-by-layer chemical exfoliation process and ZnO QDs are warped as a hybrid structure.[23]

As schematically shown in Fig. 6, we employed a layer of ZnO/G QDs as a fast electron extraction layer for the PbS CQD solar cell. In order to plot the band diagram of the PbS QD solar cell based on ZnO/G QDs, the work function and the valence band energy of the ZnO/G QDs were measured by UPS analysis and found to be 4.1 and 7.13 eV, respectively. In addition, the optical band gap of the hybrid ZnO/G QDs was calculated from UV-Vis spectra, and the energy levels of other layers were extracted following ref. 1, 22 and 25. As can be seen in Fig. 6(c), the photoinduced electrons can be smoothly transferred from the absorber layer to the hybrid QD film, which consists of n-type semiconductor particles (ZnO) with a shell of a reduced graphene oxide film, due to suitable band energy alignment. In the device structure, the photoelectrons need to flow from the reduced graphene oxide shell to the ZnO core because the energy level of ZnO is lower than graphene.[22] Furthermore, the graphene nanoshell passivates the surface dangling bonds at the interface, reducing the surface recombination.[26,27] The results of time-resolved PL spectra of the PbS QD layer deposited on the hybrid ZnO/G QD film compared with pristine ZnO nanoparticles show that, in the hybrid layer, the electron transfer occurs much faster than the radiative and/or nonradiative decay of photoexcitation; hence, the charge recombination process is significantly hindered.[18,28] Due to the electron transfer from the conduction band of the ZnO QDs (donor) to the lowest unoccupied molecular orbitals of the graphene nanoshells (acceptor), the fast deactivation of the excited state causes high charge generation efficiency.[17,29] In fact, the desirable band alignment with high conductivity of graphene facilitates efficient electron extraction and transfer in DBH colloidal QD solar cells. Consequently, an enhanced current in the external circuit, which provides higher photovoltaic performance, is attained. On the other hand, the results of *J–V* measurements for devices based on a TiO_2/ZnO layer compared with those of pristine TiO_2 and ZnO films show a higher PCE. The reduction in the recombination rate for the ZnO coated c-TiO_2 device may be attributed to the reduced injection carrier densities as opposed to improvements in the carrier lifetimes.[30] In fact, the ZnO buffer layer is introduced between TiO_2 and PbS quantum dots in order to reduce recombination and improve performance.

Conclusions

In summary, we have employed a facile chemical technique to prepare hybrid ZnO/G QDs and utilized them as a counter-electrode in DBH PbS CQD solar cells. The hybrid nanoparticles have an average size of $\sim$5 nm, with an optical bandgap of 3.24 eV. A red shift of about 50 nm in the absorption edge and large quenching in PL intensity due to warping of ZnO nanoparticles with a graphene nanoshell have been determined. It has been shown that the hybrid electrode is more efficient in electron extraction and transfer than those made of TiO_2 and TiO_2/ZnO films. An improved PCE (35%) compared to a ZnO electrode has been reported. This enhancement is supported by EQE and time-resolved PL measurements. We have suggested efficient electron injection from the conduction band of the ZnO QDs to the LUMO levels of graphene through Zn–O–C bonding and slow electron recombination.

Experimental section

Materials

Lead(II) oxide powder (PbO, 99%), oleic acid (OA, technical grade 90%), dimethyl formamide (DMF), oleylamine, anhydrous toluene, octane, methanol, isopropyl alcohol, and Triton X-100 were purchased from Merck, Germany. Graphite powder (Sigma-Aldrich), bis(trimethylsilyl) sulfide (TMS, Strem, 97% purity), 1-octadecene (ODE, Sigma-Aldrich, technical grade 90%), zinc acetate dihydrate (Sigma-Aldrich), 1,2-ethanedithiol (EDT, Sigma-Aldrich), titanium diisopropoxide bis(acetylacetonate) (75% in 2-propanol, Sigma-Aldrich), and titanium tetrachloride (Sigma-Aldrich) were used as received, without further purification.

Synthesis of graphene oxide

Graphene oxide (GO) was synthesized from graphite powder by using a modified Hummers method.[25] First, graphite powder (2.0 g) and $NaNO_3$ (1 g) were dissolved in 46 ml of H_2SO_4 at 0 °C.

Then, $KMnO_4$ (6 g) was added gradually during 2 h with stirring. The mixture was next stirred in a waterbath (30 °C) for 30 min. Then, deionized water (100 ml) was added slowly and the temperature was increased to 98 °C. The mixture was maintained at this temperature for 30 min. Finally, the reaction was terminated by adding a H_2O_2 solution (20 ml, 30%), followed by the addition of 300 ml of deionized (DI) water (Millipore, ~18 MΩ cm). The color of the mixture changed to brilliant yellow, indicating the oxidation of pristine graphite to GO. The mixture was then filtered and washed with dilute HCl to remove metal ions. The product was washed repeatedly with distilled water until the pH reached 7, and finally was dried in Petri dishes at room temperature. The atomic force microscopy (AFM) image of GO and Raman spectra of the graphitic materials are presented in the ESI,† Fig. S6.

Synthesis of PbS nanocrystals

For the synthesis of PbS nanocrystals, lead oxide (0.45 g) and ODE (3 ml) were mixed in a three-necked flask at 110 °C for 16 h. Then, 15 ml of ODE were added to the flask and a solution containing 210 μl of TMS dissolved in 10 ml of ODE was swiftly injected. The reaction product was separated by centrifugation (6000 rpm), washed several times with methanol and acetone, and re-dispersed in octane.

Cadmium doping of PbS QDs was performed according to the procedure explained in detail in the literature.[24] $CdCl_2$ (2 mmol), TDPA (0.1 g) and oleylamine (10 ml) were mixed in a flask and maintained at 100 °C for 30 min to obtain a transparent light-yellow solution. Afterward, 12 ml of octane solution of PbS QDs (80 mg ml^{-1}) were mixed with 4 ml of Cd-containing solution and maintained for 2 h, followed by washing and re-dispersion of the resultant QDs in octane.

Synthesis of hybrid zinc oxide/graphene nanocrystals

For the synthesis of hybrid zinc oxide/graphene nanocrystals, a zinc solution was prepared by dissolving 0.92 g of zinc acetate dihydrate in 200 ml of DMF. A suspension of GO in DMF (1 mg ml^{-1}) was added dropwise to the zinc solution with stirring to form a stable precursor. Afterward, this solution was heated to 95 °C and maintained at this temperature for 5 h until the color of the mixture changed to grayish-white. The obtained suspension was washed with ethanol and DI water several times by centrifugation. The final suspension contained hybrid nanocrystals dispersed in ethanol (24 mg ml^{-1}).

Fabrication of counter-electrodes

To fabricate counter-electrodes, fluorine-doped tin oxide (FTO) glass plates with an ohmic sheet resistance of 8 Ω were procured from HARTFORD GLASS, USA. The glass plates were cleaned by immersion in DI water containing 3 vol% Triton X-100 and sonicated for 30 min, rinsed with water, sonicated in isopropanol for 30 min, sonicated in a DI batch for 30 min and finally dried under nitrogen flow. A 80 nm-thick TiO_2 compact layer was deposited on the FTO substrates by spin coating (4000 rpm for 40 s) using 0.3 M solution of titanium diisopropoxide bis(acetylacetonate) (75% in 2-propanol, Sigma-Aldrich). After drying at 150 °C for 10 min, the substrates were heated at 550 °C for 30 min in air to form a compact layer of TiO_2 (c-TiO_2). Titanium chloride treatment was performed by immersing the substrates in a 50 mM $TiCl_4$ (Aldrich) aqueous solution for 30 min at 70 °C, followed by rinsing with DI water and ethanol and annealing at 550 °C for 30 min in air. A thin layer of hybrid ZnO/G QDs was then deposited on c-TiO_2 by the cathodic electrophoretic deposition (EPD) technique. The EPD cell consisted of a c-TiO_2-coated FTO electrode and a carbon rod counter-electrode positioned parallel to each other with a 10 mm distance, and the ZnO/G suspension (24 mg ml^{-1}). A DC voltage of 100 V was applied for 10 min. After deposition, the electrode was washed with DI water and dried by a flow of nitrogen gas. Finally, the samples were annealed on a hot plate at 120 °C for 1 h. The thickness of the ZnO/G layer was optimized based on the transmittance of the electrodes and performance of the CQD solar cells. It has been found that the thickness of the hybrid ZnO/G layer should be around 100 nm to gain high transparency with improved solar conversion efficiency. In order to explore the role of the graphene nanoshell and the compact layer, some electrodes were also prepared by utilizing chemically processed ZnO nanoparticles (without a graphene shell), which were prepared according to the procedure explained in the literature,[31–35] on the surface of the FTO and FTO/c-TiO_2 substrates. Therefore, four types of counter-electrode materials were prepared and utilized: FTO/ZnO, FTO/c-TiO_2, FTO/c-TiO_2/ZnO, and FTO/c-TiO_2/hybrid QDs.

Material characterization

The following section discusses the characterization of materials in our study. A high-resolution transmission electron microscope (HRTEM, JOL, JEM-2100, Japan) equipped with an energy-dispersive X-ray spectroscope (EDS) was used for structural studies. For phase characterization, X-ray diffraction (XRD, Stone Sandi P, USA) using Cu Kα radiation was employed. Infrared spectra were recorded on a Perkin-Elmer Fourier transform infrared spectrometer (FTIR, Spectrum RX, USA). An InVia spectrometer (Renishaw AB, Sweden) with a 514.5 nm wavelength incident laser light was used to record the Raman spectra. X-ray photoelectron spectroscopy (XPS) measurements were carried out on a hemispherical analyzer with an Al Kα X-ray source (1486.6 eV) operated at 10^{-7} Pa. Optical studies (absorption and photoluminescence (PL) spectra) were performed on a Varian Cary 500 spectrometer (Varian, USA) and a FLS920P fluorescence spectrometer (Edinburgh Instruments) equipped with a cryogenically cooled photomultiplier (R5509-43, Hamamatsu), with a 450 W continuous xenon arc lamp as the excitation source for steady-state spectra. PL decay curves were fitted using the stretched exponential function $I(t) = I_0 e^{-(t/\tau)^{\beta}}$, where β is a stretch parameter and τ is the decay time. The photoluminescence quantum yield (PLQY), defined as the ratio of photons emitted to photons absorbed by the sample, was determined by an absolute method using the same fluorescence spectrometer equipped with an integrating sphere and a BENFLECR coated inner face (Edinburgh Instruments Ltd, UK). The excitation source for these measurements was the

spontaneous emission from a steady-state 500 mW/685 nm DPSS laser operating just below the lasing threshold. The spectral correction curve, which takes account of the sensitivity of the monochromator, detector, sphere coating and optics to the wavelength, was provided by Edinburgh Instruments Ltd. The thickness, morphology and roughness of the films were studied by field-emission scanning electron microscopy (FESEM, Hitachi S4160, Japan) and atomic force microscopy (AFM, JPK Co, Germany). The work function and the valence band of the semiconducting ZnO/G layer were obtained by ultraviolet photoelectron spectroscopy (UPS, AXIS NOVA, Kratos Analytical Ltd, UK) by employing He I (21.2 eV) as the photon source.

Device fabrication and photovoltaic measurements

DBH solar cells were fabricated *via* layer-by-layer deposition of the Cd-doped PbS colloidal solution on the hybrid ZnO/G electrodes by employing the spin-coating process. In order to replace the long OA ligand with the short thiol molecules of EDT, a solid-state ligand exchange process was employed. In the process, after spin-coating PbS QDs at 2500 rpm for 30 s, an EDT solution (1 vol% in anhydrous methanol) was spread on the surface for 3 s, spin-cast (2500 rpm) for 10 s, and finally washed with anhydrous methanol twice. This process was repeated for 10 runs until a uniform film of $\sim$300 nm thickness was obtained. The electrodes were finally dried in a nitrogen-filled glove box. To complete the device fabrication, the top contact, consisting of MoO_3/Au layers (25 nm/100 nm), was deposited by thermal evaporation at a rate of 0.8 Å s^{-1}.

The solar spectrum at AM 1.5G was simulated with a Xe lamp and filters with an intensity of 100 mW cm^{-2}. The current–voltage (*J*–*V*) data were measured using a Keithley 2400 (USA) instrument. *J*–*V* sweeps were performed between −1 and +1 V, with a step size of 0.02 V and a delay time of 150 ms at each point. The accuracy of the power measurement was estimated to be ±5%. The average values of measurements on different devices (n = 10) were reported as the PCE value of each solar cell. External quantum efficiency (EQE) spectra were recorded as a function of wavelength under a constant white light bias of approximately 5 mW cm^{-2} supplied by an array of white light-emitting diodes. The excitation beam coming from a 300 W xenon lamp (ILC Technology, Inc, USA) was focused through a Gemini-180 double monochromator (HORIBA Jobin Yvon IBH Ltd, Japan) and chopped at approximately 2 Hz. The signal was recorded using a Model SR830 DSP Lock-In Amplifier.

Acknowledgements

This work was supported by the General Research Fund (project 612113) of the Hong Kong Research Grants Council and the Hong Kong Innovation and Technology Fund (project ITS/117/13) of the Innovation and Technology Commission. AS is also thankful for funding support from the Grant Program of Sharif University of Technology (No. G930305) and the Elite National Institute.

Notes and references

1 J. Y. Kim, O. Voznyy, D. Zhitomirsky and E. H. Sargent, *Adv. Mater.*, 2013, **25**, 4986–5010.
2 D. V. Talapin, J. S. Lee, M. V. Kovalenko and E. V. Shevchenko, *Chem. Rev.*, 2009, **110**, 389–458.
3 M. M. Tavakoli, A. Simchi and H. Aashuri, *Mater. Chem. Phys.*, 2015, **156**, 163–169.
4 A. Tayyebi, M. M. Tavakoli, M. Outokesh, A. Shafiekhani and A. Simchi, *Ind. Eng. Chem. Res.*, 2015, **54**, 7382–7392.
5 S. A. McDonald, G. Konstantatos, S. Zhang, P. W. Cyr, E. J. Klem, L. Levina and E. H. Sargent, *Nat. Mater.*, 2005, **4**, 138–142.
6 P. T. Erslev, H.-Y. Chen, J. Gao, M. C. Beard, A. J. Frank, J. van de Lagemaat, J. C. Johnson and J. M. Luther, *Phys. Rev. B: Condens. Matter Mater. Phys.*, 2012, **86**, 155313.
7 J. Gao and J. C. Johnson, *ACS Nano*, 2012, **6**, 3292–3303.
8 Z. Ning, O. Voznyy, J. Pan, S. Hoogland, V. Adinolfi, J. Xu, M. Li, A. R. Kirmani, J. Sun, J. Minor, K. W. kemp, H. Dong, L. Rollny, A. Labelle, G. Carey, B. Sutherland, I. Hill, A. Amassian, H. Liu, J. Tang, O. M. Bakr and E. H. Sargent, *Nat. Mater.*, 2014, **13**, 822–828.
9 X. Lan, J. Bai, S. Masala, S. M. Thon, Y. Ren, I. J. Kramer, S. Hoogland, A. Simchi, G. I. Koleilat, D. Paz-Soldan, Z. Ning, A. J. Labelle, J. Young Kim, G. Jabbour and E. H. Sargent, *Adv. Mater.*, 2013, **25**, 1769–1773.
10 A. J. Labelle, S. M. Thon, S. Masala, M. M. Adachi, H. Dong, M. Farahani, A. H. Ip, A. Fratalocchi and E. H. Sargent, *Nano Lett.*, 2014, **15**, 1101–1108.
11 M. M. Tavakoli, H. Aashuri, A. Simchi, S. Kalytchuk and Z. Fan, *J. Phys. Chem. C*, 2015, **119**, 18886–18895.
12 P. Avouris, Z. Chen and V. Perebeinos, *Nat. Nanotechnol.*, 2007, **2**, 605–615.
13 V. Yong and J. M. Tour, *Small*, 2010, **6**, 313–318.
14 A. K. Geim and K. S. Novoselov, *Nat. Mater.*, 2007, **6**, 183–191.
15 G. Konstantatos, M. Badioli, L. Gaudreau, J. Osmond, M. Bernechea, F. G. Arquer, F. Gatti and F. H. K. Koppens, *Nat. Nanotechnol.*, 2012, **7**, 363–368.
16 D. Zhang, L. Gan, Y. Cao, Q. Wang, L. Qi and X. Guo, *Adv. Mater.*, 2012, **24**, 2715–2720.
17 M. Eck, C. V. Pham, S. Züfle, M. Neukom, M. Sessler, D. Scheunemann, E. Erdem, S. Weber, H. Borchert, B. Ruhstaller and M. Kruger, *Phys. Chem. Chem. Phys.*, 2014, **16**, 12251–12260.
18 M. M. Tavakoli, A. Tayyebi, A. Simchi, H. Aashuri, M. Outokesh and Z. Fan, *J. Nanopart. Res.*, 2015, **17**, 1–13.
19 D. I. Son, B. W. Kwon, Y. J. Do, D. H. Park, W. S. Seo, H. Lee, Y. Yi, C. L. Lee and W. K. Choi, *Nano Res.*, 2012, **5**, 747–761.
20 J. T. W. Wang, J. M. Ball, E. M. Barea, A. Abate, J. A. Alexander-Webber, J. Huang, M. Saliba, I. Mora-Sero, J. Bisquert, H. J. Snaith and R. J. Nicholas, *Nano Lett.*, 2013, **14**, 724–730.
21 Z. Zhu, J. Ma, Z. Wang, C. Mu, Z. Fan, L. Du, Y. Bai, L. Fan, H. Yan, D. L. Phillips and S. Yang, *J. Am. Chem. Soc.*, 2014, **136**, 3760–3763.
22 D. I. Son, B. W. Kwon, J. D. Yang, D. H. Park, W. S. Seo, H. Lee, Y. Yi, C. L. Lee and W. K. Choi, *Nat. Nanotechnol.*, 2012, **7**, 465–471.

23 D. I. Son, B. W. Kwon, J. D. Yang, D. H. Park, W. S. Seo, H. Lee, Y. Yi, C. L. Lee and W. K. Choi, *Nano Res.*, 2012, **5**, 747–761.
24 S. Niyogi, E. Bekyarova, M. E. Itkis, J. L. McWilliams, M. A. Hamon and R. C. Haddon, *J. Am. Chem. Soc.*, 2006, **128**, 7720–7721.
25 A. H. Ip, S. M. Thon, S. Hoogland, O. Voznyy, D. Zhitomirsky, R. Debnath, L. Levina, A. Fischer, K. W. Kemp, I. J. Kramer, Z. Ning, A. J. Labelle, K. W. Chou, A. Amassian and E. H. Sargent, *Nat. Nanotechnol.*, 2012, **7**, 577–582.
26 D. A. Neamen, *Semiconductor Physics and Devices*, McGraw-Hill, New York, NY, 3rd edn, 2003.
27 J. O. Hwang, D. H. Lee, J. Y. Kim, T. H. Han, B. H. Kim, M. Park, K. No and S. O. Kim, *J. Mater. Chem.*, 2011, **21**, 3432–3437.
28 D. Zhang, L. Gan, Y. Cao, Q. Wang, L. Qi and X. Guo, *Adv. Mater.*, 2012, **24**, 2715–2720.
29 K. T. Nguyen, D. Li, P. Borah, X. Ma, Z. Liu, L. Zhu, G. Grüner, Q. Xiong and Y. Zhao, *ACS Appl. Mater. Interfaces*, 2013, **16**, 8105–8110.
30 K. W. Kemp, J. L. Andre, M. T. Susanna, A. H. Ip, I. J. Kramer, S. Hoogland and E. H. Sargent, *Adv. Energy Mater.*, 2013, **7**, 917–922.
31 Y. Gao, H. Jin, Q. Lin, X. Li, M. M. Tavakoli, S. Leung, W. M. Tang, L. Zhou, H. L. Chan and Z. Fan, *J. Mater. Chem. A*, 2015, **3**, 10199–10204.
32 M. M. Tavakoli, R. Tavakoli, P. Davami and H. Aashuri, *J. Comput. Electron.*, 2014, **13**, 425–431.
33 M. M. Tavakkoli and S. M. Abbasi, *Mater. Des.*, 2013, **46**, 573–578.
34 T. V. Cuong, V. H. Pham, J. S. Chung, E. W. Shin, D. H. Yoo, S. H. Hahn and J. S. Huh, *Mater. Lett.*, 2010, **22**, 2479–2482.
35 K. F. Lin, H. M. Cheng, H. C. Hsu, L. J. Lin and W. F. Hsieh, *Chem. Phys. Lett.*, 2005, **409**, 208–211.